Extremely suppressed thermal conductivity of large-scale nanocrystalline silicon through inhomogeneous internal strain engineering

Bin Xu[a,b], Yuxuan Liao[a], Zhenglong Fang[a], Yifei Li[a], Rulei Guo[a], Ryohei Nagahiro[a], Yoshifumi Ikoma[c], Masamichi Kohno[d,e], Junichiro Shiomi[a,b*]

[a]*Department of Mechanical Engineering, The University of Tokyo, 7-3-1 Hongo, Bunkyo, Tokyo 113-8656, Japan.*
[b]*Institute of Engineering Innovation, The University of Tokyo, 2-11 Yayoi, Bunkyo, Tokyo 113-8656, Japan*
[c]*Department of Materials Science and Engineering, Kyushu University, 744 Motooka, Nishi-ku, Fukuoka, 819-0395, Japan*
[d]*Department of Mechanical Engineering, Kyushu Universi ty, 744 Motooka, Nishi-ku, Fukuoka 819-0395, Japan*
[e]*International Institute for Carbon-Neutral Energy Research (WPI-I2CNER), Kyushu University, 744 Motooka, Nishi-ku, Fukuoka 819-0395, Japan*
[*]*E-mail: shiomi@photon.t.u-tokyo.ac.jp*

SI: Method

1 Sample preparation

1.1 Plasma sintering

Silicon nanoparticles with a diameter of 30 nm (Guangzhou Hongwu Material Technology Co., Ltd) and 0.5 wt% silver nanoparticles with a diameter of 100 nm (Sigma-Aldrich) were used to fabricate the nanocrystal silicon composite by a plasma sintering method (ELENIX, ED-PAS). The primary sintering was performed by a typical plasma sintering process (sintering pressure, approximately 40 MPa) at 1000 °C in a vacuum chamber (pressure, approximately 5 Pa) after a pulse plasma treatment (time, 150 s; current, 200 A; voltage, 2 V). The pulse plasma treatment removes the natural oxide layer of the silicon particles. The diameter and thickness of the nanocrystal silicon composite was 10, and approximately 2–3 mm, respectively. Three samples with similar κ_L values of 2.2–2.65 W/m-K (measured by laser flash) were prepared for HPT processing.

1.2 HPT process

Herein, tungsten carbide anvils having a shallow hole with a diameter of 10 mm and depth of 0.25 mm were used for HPT. The sintered silicon sample was set at the center of the anvil and then loaded to 490 kN within 7 s, which provided a nominal pressure of approximately 6 GPa. Subsequently, torsional shear strain was applied by rotating the lower anvil at a speed of 1 rpm with the upper anvil fixed. When the rotation reached the predetermined value, the sample was unloaded to ambient pressure in 2 s and reformed to the elastic regime. Details regarding the HPT instrument and process have been described in previous studies and can be found there [1–3]. After the HPT process, the sample was initially measured by the laser flash to obtain the overall thermal conductivity and then polished to a mirror-like surface with a roughness of several nanometers by a CMP process for the following Raman and time-domain thermoreflectance (TDTR) characterizations. Further, it underwent ion-milling for the electron backscatter diffraction pattern (EBSD) measurement.

2 Thermal conductivity measurement

2.1 LFA

Laser flash (NETZSCH, LFA447) was used to characterize the thermal diffusivity of the entire sample. Both sides of the sample were treated with graphite spray to enhance heat absorption and irradiation. The measurement was performed three times at different temperatures ranging from 23 to 500 °C inside a vacuum chamber. A monolayer crown model was used to analyze the temperature variation to extract the thermal diffusivity. Further, the κ_L value was calculated using the density measured by the Archimedes method and the theoretical heat capacity.

2.2 TDTR

A typical TDTR setup was used to explore the microscale thermal conductivity distribution of the HPT sample [4–6]. In brief, an 800-nm laser with a pulse width of 170 fs and frequency of 80 MHz was used as the laser source. The laser was further divided into two paths, for probing and pumping: one path was by changing the laser to 400 nm by BIBO and modulating under a frequency of 11 MHz to heat the sample surface; the other path passed through the delay stage to probe the temperature at the sample surface under a certain time delay. A temperature decay profile varying from 0 to 8 ns can be obtained by a continuously varied delay stage position. For sample preparation, an aluminum transducer layer with a thickness of 70 nm was deposited on the sample's surface using a vacuum evaporator. The thermal properties, such as κ_L, can be extracted from the temperature decay profile by fitting the experimental curve to the theoretical heat conduction model described by the Fourier transport equation. In this case, a two-layer model (aluminum/silicon) was used in the analysis. To guarantee the reliability of the targeted κ_L of the silicon layer (κ_{Si}), sensitivity calculation was performed (Fig. S5 (a)), where the sensitivity of κ_{Si} was high. A typical experimental temperature decay profile ($-V_{in}/V_{out}$) and the fitting curve is shown in Fig. S5(b), where the differences in κ_{Si} can lead to significant differences in temperature decay. The parameters for TDTR analysis are summarized in Table S1.

3 Structural characterizations

3.1 XRD measurement

An X-ray diffraction (XRD; Rigaku, SmartLab) equipment equipped with a Cu Kα source was used to determine the grain size and internal strain through Williamson–Hall analysis. To obtain the peak broadening (β_{total}) parameter, the XRD spectrum was fitted with pseudo-Voigt functions to determine the peak's position and obtain the bandwidth ($\beta_{measure}$) from the area-to-height ratio [7]. Fig. S5 shows the fitting result of 1/2 rotation samples. In addition, to exclude the contribution of the instrument to peak broadening, a standard polycrystal silicon sample (purchased from Kojundo Chemical) was measured and the bandwidth of individual peaks ($\beta_{standard}$) was obtained. Consequently, the structure-originated peak broadening (β_{total}) could be calculated by $\beta_{total} = \beta_{measure} - \beta_{standard}$. Further, the internal strain ($C\varepsilon$) and grain size (D) can be separately determined as the angle-dependent peak broadening ($\beta_{total} = \beta_\varepsilon + \beta_L$) originating from inhomogeneous internal strain ($\beta_\varepsilon = C\varepsilon \tan\theta$) is different from the average grain size ($\beta_L = K\lambda/D\cos\theta$), where K is a constant (often taken as 0.9), and λ is the wavelength of the X ray-source ($\lambda = 0.15418$ nm for CuKα source). By fitting the experimental β_{total} with the equation $\beta_{total}\cos\theta = C\varepsilon\sin\theta + K\lambda/D$, the corresponding internal strain from the slope ($C\varepsilon$)) and the grain size information from the intercept ($K\lambda/L$) were obtained.

3.2 Raman spectroscopy

Raman spectroscopic measurements (inVia, Renishaw) were used to identify the internal stress. A 532-nm laser and grating of 3000 were applied to guarantee a high wavenumber resolution of 0.02 cm^{-1}. An objective lens (50×) was used to achieve a laser beam size of approximately 500 nm. The laser power was adjusted to 1.91 mW to avoid any unnecessary shift of the Raman peak caused by heating.

3.3 Acoustic velocity measurements

The sound velocity of a material (v_S) can be calculated from the longitude (v_L) and transverse (v_T) acoustic velocity. The acoustic velocity measurement was performed using an ultrasonic gauge (Olympus 38DL PLUS) equipped with a longitudinal (v1091) and transverse (v157) wave probe, whose working frequencies were both 5 MHz. The sound velocity was calculated from the time interval between the initial pulse and second reflected signals. A pristine silicon single-crystal sample with an LA, TA, and resultant sound velocity of 9244, 5843, and 6429 m/s, respectively, was used as the reference. This sound velocity was also used to calculate κ_L for calibrating the phonon group velocity.

3.4 SEM/EBSD measurement

For the grain crystallographic observation, an ion beam was used to mill the cross-section of the sample to obtain a finely polished surface without introducing additional stress. Next, the crystallographic orientation and nanograin distribution were obtained by field emission scanning electron microscopy using the EBSD method. (JSM-7100F, JEOL Ltd.; emission current, 63 μA; acceleration voltage, 15 kV; working distance, 25 mm; scanning step size, 10 nm). The silicon lattice structure was set to identify the Kikuchi diffraction pattern with a confidential index of over 0.5, followed by the orientation data conversion to the raw binary data for further nanograin analysis. Standard kernel average misorientation (KAM) and grain reference orientation deviation (GROD) orientation were derived from the crystallographic orientation distribution for assessing the plastic deformation level and the residual strain at the interior of individual grains. We specify the detected spot orientation as reference frame, and then compute the product of an inverse orientation with another orientation, thereby transferring crystal coordinates. Based on this transformation operation, we derive the misorientation angle.

4 Thermal conductivity calculation

4.1 Thermal conductivity calculation

The phonon properties include the phonon group velocity (v_s), state density (D_s) and relaxation time (τ) obtained through a first-principles-based anharmonic lattice dynamics calculation and were inserted into equation (2) to calculate the κ_L. As the strain resulted in a significant reduction in phonon group velocity (v_s), the phonon group velocity (v_s) was calibrated based on the sound velocity measurement result using $v_g/v_{g0} = v_s/v_{s0}$. Regarding the relaxation time, as

the sample is pure silicon without any impurities, such as a metastable phase or dopant and pores (the relative density is almost 100%), only phonon–phonon and phonon–boundary scatterings (equation (3)) were considered. The relaxation time of phonon–phonon scattering was calibrated by the sound velocity, as given by equations (4) and (5), whereas that of phonon–boundary scattering is given by equation (6).

4.2 Atomistic Green's function calculation (AGF)

The phonon transmission and thermal resistance term γ of the silicon/silicon interface with a softening interfacial layer were calculated by the atomistic Green's function (AGF) method using the Quantum ATK package. The interfacial structure for the AGF calculation comprises three components (Fig. S7 (a)): softened silicon with modified modulus in the middle, and pristine Si (semi-infinite length) with standard modulus on the left (L) and right (R) sides of the interface (C). Tersoff potentials were employed to describe the interatomic interaction in the system. By tuning the parameters of A and B in the Tersoff potential [8] function, the lattice stiffness of the silicon interfacial layer could be modified to simulate the interfacial softening. Herein, three cases of interfacial thickness were calculated, with an elastic modulus in the Z direction (heat conduction direction) ranging from 168.0 to 12.9 GPa by varying A and B according to Table S2. The mixing rule was used to model the interactions between the silicon atoms on the right/left and center with different force potential settings. Before the primary AGF calculation at 300 K to obtain the thermal boundary conductance (TBC), the structure was first optimized with the aforementioned potential to ensure that the stress tolerance was less than 0.01 GPa and force tolerance was smaller than 0.005 eV/Å. Using this model, the AGF calculation was performed for systems under different interfacial condition settings, as described above. Evidently from Fig. S7(b), the theoretical curve fit the calculated phonon transmittance well and could yield the value of gamma.

SI: Additional Discussion

1 The impurities in HPT and their influence on the thermal conductivity

Regarding the minor component of graphite and silver detected by XRD, they influence on thermal conductivity is negligible. The graphite impurities were introduced during sintering because we used a graphite die and electrode. Therefore, these graphite impurities are mainly distributed on the surface of the samples and do not influence the bulk thermal conductivity. Silver nanoparticles (with a diameter of 100 nm and concentration of 0.5 wt%) were added to the silicon nanoparticles upon sintering following our previous study[9], where silver was expected to contribute to the enhancement of power factor. However, for thermal conductivity, which is the focus of this work, the small amount of silver has negligible influence because the phonon scattering rate (τ_{Ag}^{-1}) by silver particles is more than three orders of magnitudes smaller than the overall effective phonon scattering rate of HPT samples (τ_{eff}^{-1}). This can be shown by taking the extreme scenario assuming silver particles to be voids of the same size and density, where the scattering rate is calculated based on the geometrical scattering model[10]:

$$\tau_{Ag}^{-1} = \frac{n}{\sigma_s^{-1} + \sigma_l^{-1}} v_g$$

where σ_s and σ_l are the cross-sections of geometrical scattering in the limits of short and long wavelength, respectively[11]. n is the number density of Ag nanoparticles, expressed as $3vol/4\pi r^3$. σ_s can be expressed as $2\pi r^2$. r and vol are the radius and volume fraction of silver, respectively. Since the $\sigma_s \ll \sigma_l$, the contribution from σ_l is negligible in the calculation. Using the phonon group velocity (v_g) obtained from the lattice dynamic calculation, the τ_{Ag}^{-1} can be obtained through $\tau_{Ag}^{-1} = v_g \Lambda_{Ag}^{-1}$. As illustrated in Fig. S10, τ_{Ag}^{-1} is three orders of magnitude smaller than the τ_{eff}^{-1} of 1/2 rotation HPT samples. Overall, these results indicate that the impurities scattering by the silver are negligible when discussing HPT silicon's thermal conductivity.

2 The electronic thermal conductivity

We measured the electrical conductivity using the 4-probe method. The results are shown in Fig. S8. The figure shows nonlinear dependence of electrical conductivity on the degree of rotation; however, since there is no assurance that such a trend would sustain when samples are doped, we did not discuss the results in the context of thermoelectrics. Using this electrical conductivity, we calculated the thermal conductivity contributed by the charge carrier using Wiedemann–Franz law: $\kappa_e = LT\sigma$. Herein, T is the temperature, σ is the electrical conductivity, and L is the Lorentz number, which is a constant at a given temperature, and is set to 2.44×108

W-Ω-K^{-2} for the room temperature case. Using the electrical conductivity measured by the 4-probe method (Fig. S8), the electronic thermal conductivity at room temperature can be obtained, which ranges from 0.0033 to 0.0072 W/m-K. This electronic thermal conductivity is about three orders of magnitude smaller than the phonon thermal conductivity; thus, it is negligible in the thermal conductivity analysis.

3 The thermal stability of the HPT samples

We measured temperature-dependent thermal conductivity from room temperature to 300 ^{o}C. Even after the measurement at 300 ^{o}C that lasted for about 3 h, we observed no substantial change in the thermal conductivity. Furthermore, all the strain characterization was performed after the thermal conductivity measurement at 300 ^{o}C and confirmed the presence of strong strain. These indicate that the strain generated by the HPT process is effectively stable at least below 300 ^{o}C.

SI Figures

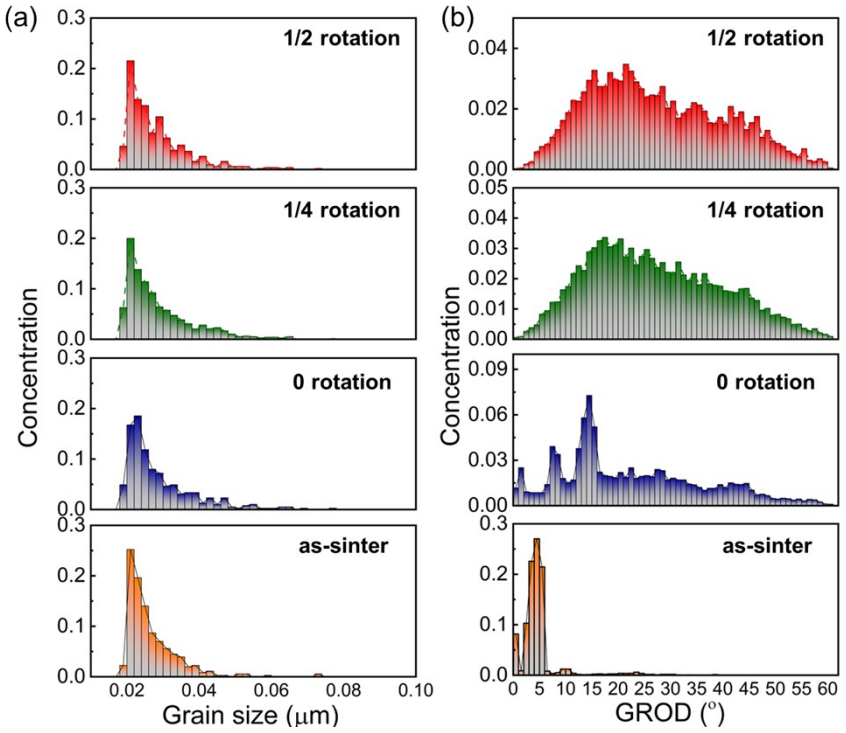

Figure S1 Result of EBSD analysis. (a) grain size distribution, and (b) GROD histogram of as-sinter and 0, 1/2, 1/4 rotation HPT sample.

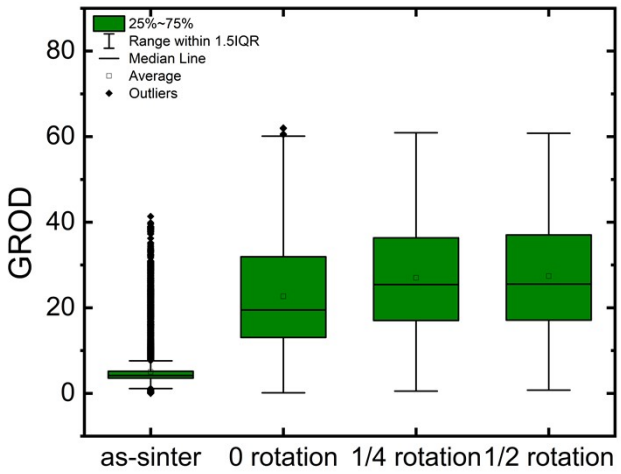

Figure S2. The GROD distribution of HPT samples.

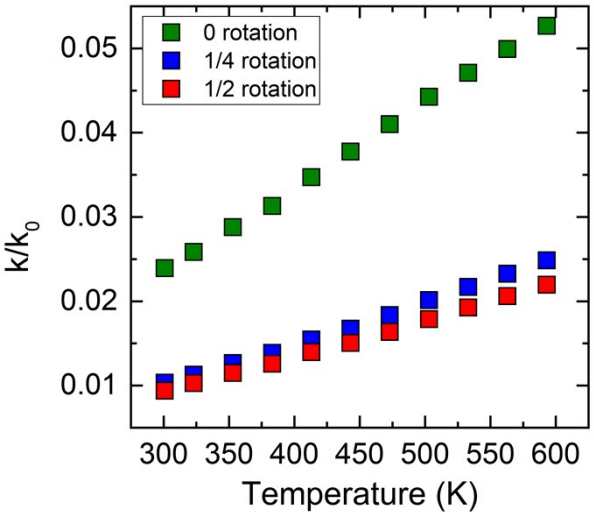

Figure S3. Normalized thermal conductivity of HPT samples under different temperatures.

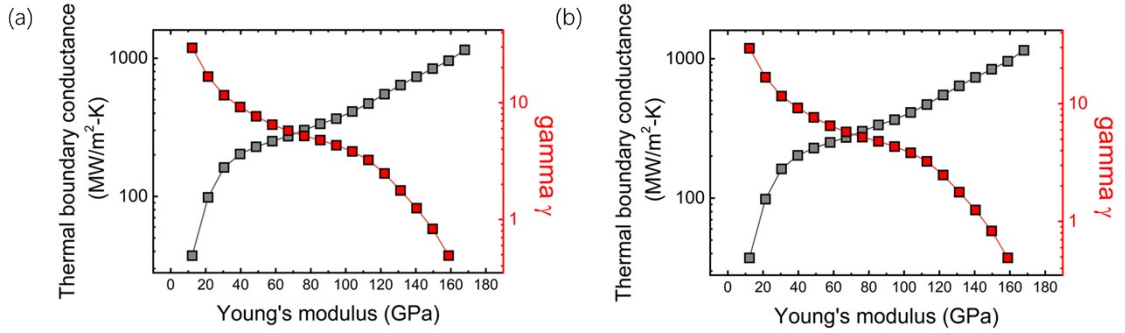

Figure S4. Thermal boundary conductance and the gamma of samples with different Young's modulus with interfacial layer thickness of (a) 3nm, and (b) 7.5 nm.

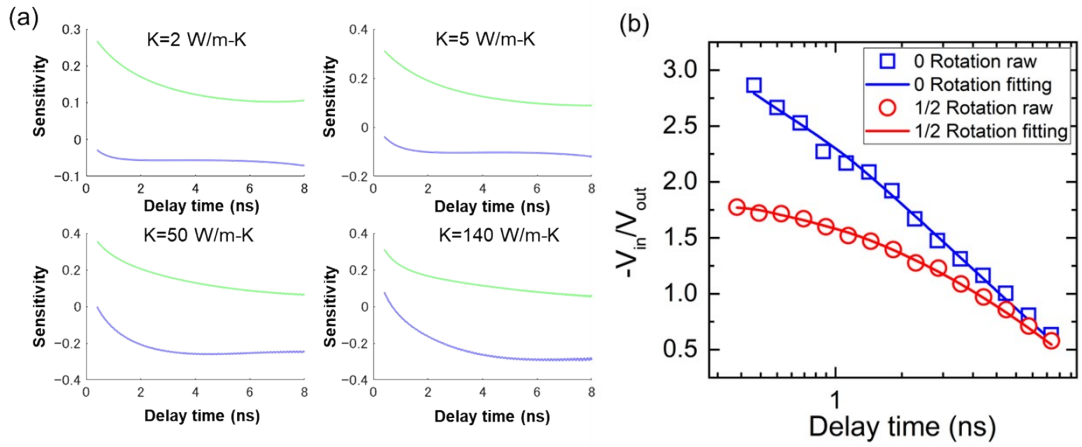

Figure S5 TDTR measurement. (a) The sensitivity calculation of Al/Si system under different thermal conductivity of Si layer; The blue curves represent the thermal boundary conductance of Al/Si interface, and the green curves represent the thermal conductivity of the silicon layer. (b) The temperature decay signal ($-V_{in}/V_{out}$) and the fitting result of 0 and 1/2 rotation sample.

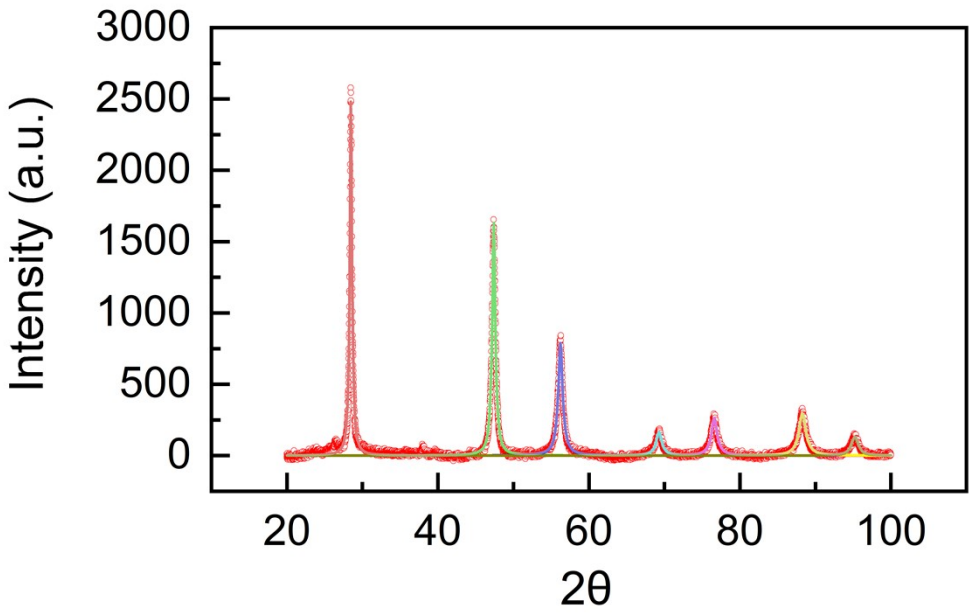

Figure S6. A representative XRD spectrum fitting for Williamson-Hall analysis; 1/2 rotation sample.

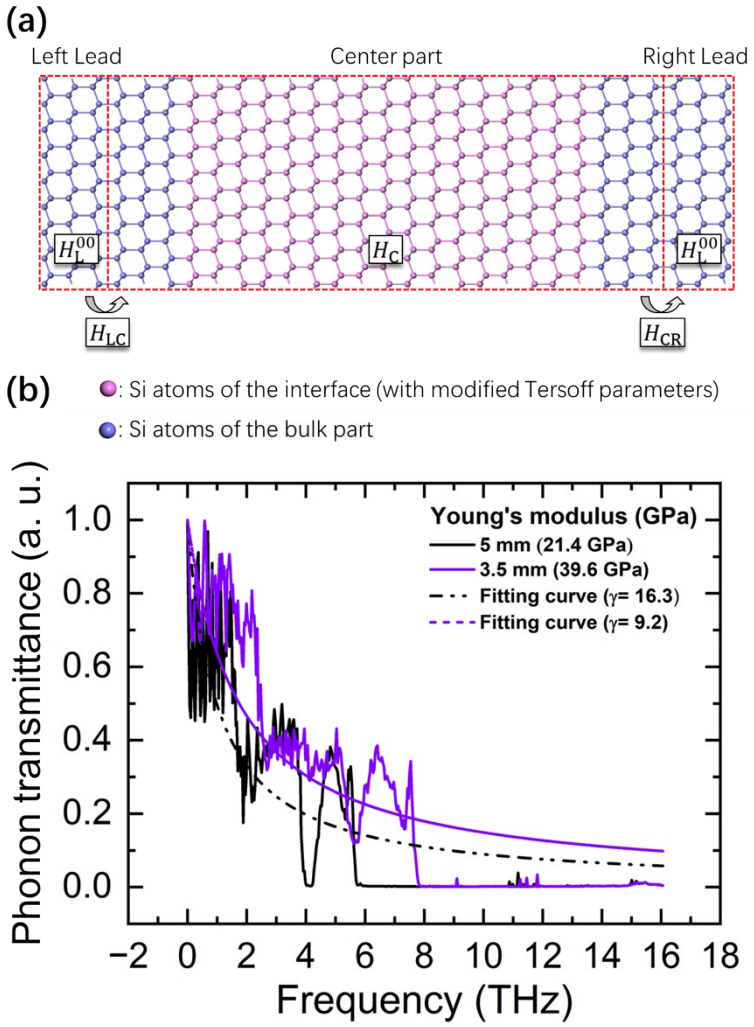

Figure S7. AFG calculation. (a) The schematic of the model used in the AGF calculation. H_L^{00},H_L^{00},H_C,H_{LC}, H_{CR} indicates the interaction matrix of different locations of the system. (b) The phonon transmittance and the fitting curve for obtaining γ in cases of 5mm interfacial layer, 21.4 GPa young's modulus, and 3.5mm interfacial layer, 39.6 GPa young's modulus.

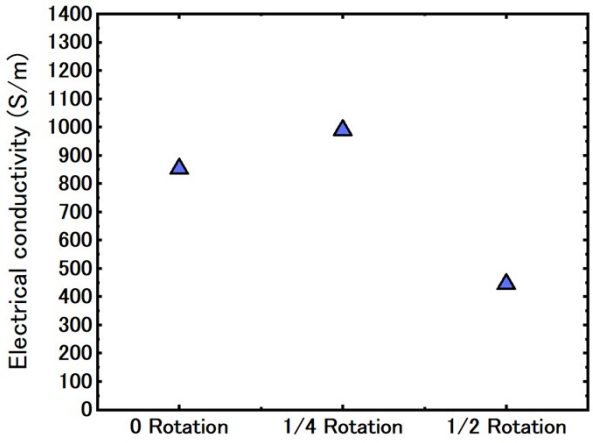

Figure S8. The electrical conductivity of the HPT samples.

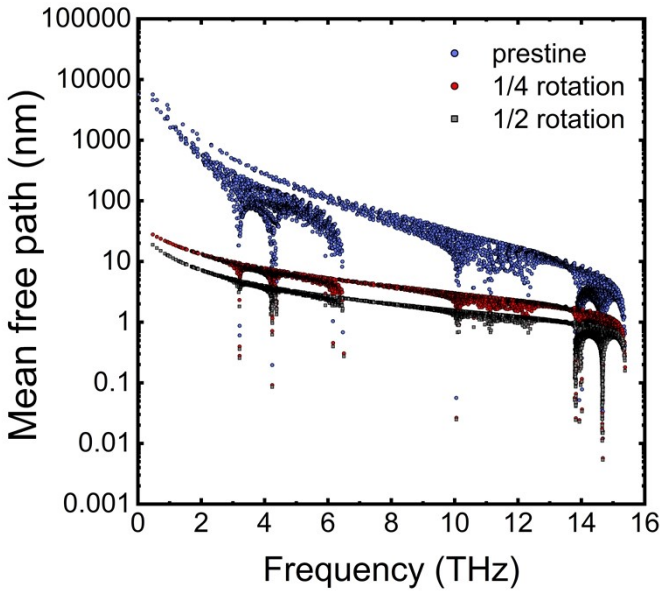

Figure S9. The phonon MFP of pristine silicon and HPT-processed silicon with 1/4 and 1/2 rotation.

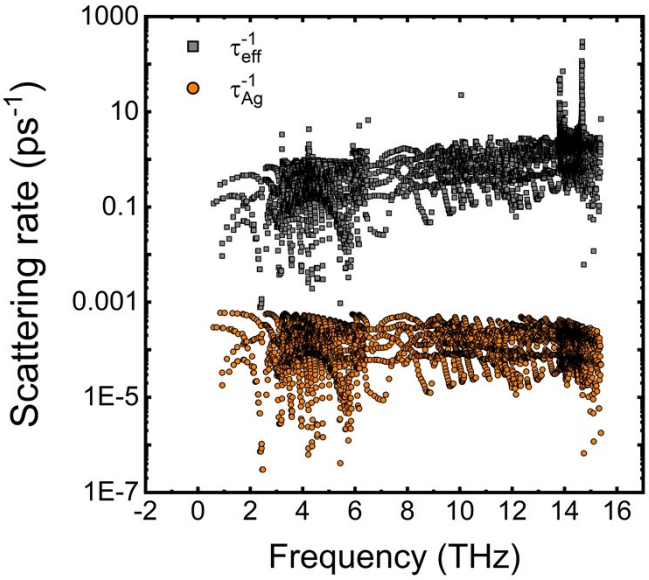

Figure S10. The geometrical phonon scattering rate by Ag nanoparticles and the overall effective phonon scattering rate of HPT processed silicon under 1/2 rotation.

SI Tables

Table S 1. The parameters used for TDTR analysis and sensitivity calculation.

Properties	**Layer 1 (Al)**	**Layer 2 (Si)**
Thermal conductivity (W/m-K)	97.2	-
Cp (J/m^3-K)	2.42	1.6
Thickness (nm)	69.2	5E5

Table S 2. The parameters modification of Tersoff potential and the corresponding Young's modulus

	Tersoff potential		**Young's modulus (@different Direction)**		
case No	**A**	**B**	**X**	**Y**	**Z**
PR-1	1830.8	471.18	137.9548	138.0189	167.9609
PR-2	1730.918	445.4742	130.4285	130.4891	158.7976
PR-3	1631.037	419.7684	122.9022	122.9593	149.6343
PR-4	1531.155	394.0626	115.3759	115.4295	140.471
PR-5	1431.274	368.3568	107.8496	107.8997	131.3076
PR-6	1331.392	342.651	100.3233	100.3699	122.1443
PR-7	1231.511	316.9451	92.7737	92.8639	112.9255
PR-8	1131.629	291.2393	85.2493	85.3321	103.7667
PR-9	1031.747	265.5335	77.7249	77.8004	94.6079
PR-10	931.8658	239.8277	70.2573	70.3108	85.449
PR-11	831.9842	214.1219	62.7268	62.7746	76.2902
PR-12	732.1026	188.4161	55.1518	55.2474	67.133
PR-13	632.221	162.7103	47.6019	47.6937	58.0337
PR-14	532.3395	137.0045	40.1364	40.1776	48.8263
PR-15	432.4579	111.2987	32.6057	32.6392	39.6652
PR-16	332.5763	85.59285	25.075	25.1008	30.504
PR-17	232.6947	59.88704	17.5553	17.5495	21.3688
PR-18	132.8131	34.18123	10.0668	9.9887	12.2872

Reference

1 Y. Fukushima, Y. Ikoma, K. Edalati, B. Chon, D. J. Smith and Z. Horita, *Mater. Charact.*, 2017, **129**, 163–168.

2 Y. Ikoma, K. Hayano, K. Edalati, K. Saito, Q. Guo and Z. Horita, *Appl. Phys. Lett.*, 2012, **101**, 121908.

3 Y. Ikoma, T. Yamasaki, T. Shimizu, M. Takaira, M. Kohno, Q. Guo, M. R. McCartney, D. J. Smith, Y. Arai and Z. Horita, *Mater. Charact.*, 2020, **169**, 110590.

4 B. Xu, S. Hu, S. W. Hung, C. Shao, H. Chandra, F. R. Chen, T. Kodama and J. Shiomi, *Sci. Adv.*, 2021, **7**, eabf8197.

5 B. Xu, S.-W. Hung, S. Hu, C. Shao, R. Guo, J. Choi, T. Kodama, F.-R. Chen and J. Shiomi, *Carbon N. Y.*, 2021, **175**, 299–306.

6 F. Mu, B. Xu, X. Wang, R. Gao, S. Huang, K. Wei, K. Takeuchi, X. Chen, H. Yin, D. Wang, J. Yu, T. Suga, J. Shiomi and X. Liu, *J. Alloys Compd.*, 2022, **905**, 164076.

7 R. Hanus, M. T. Agne, A. J. E. Rettie, Z. Chen, G. Tan, D. Y. Chung, M. G. Kanatzidis, Y. Pei, P. W. Voorhees and G. J. Snyder, *Adv. Mater.*, 2019, **31**, 1–10.

8 J. Tersoff, *Phys. Rev. B*, 1989, **39**, 5566–5568.

9 M. Kashiwagi, Y. Liao, S. Ju, A. Miura, S. Konishi, T. Shiga, T. Kodama and J. Shiomi, *ACS Appl. Energy Mater.*, 2019, **2**, 7083–7091.

10 M. Kashiwagi, Y. Sudo, T. Shiga and J. Shiomi, *Phys. Rev. Appl.*, 2018, **10**, 044018.

11 W. Kim and A. Majumdar, *J. Appl. Phys.*, 2006, **99**, 044018.